Electronic Supplementary Information

Wood modification for the synthesis of MOF@wood composite materials with increased metal organic framework (MOF) loading

Alex Spieß[1], Janis Wiebe[1], Egor Iwaschko[1], Dennis Woschko[1] and Christoph Janiak*,[1]

[1] Institut für nanoporöse und nanoskalierte Materialien, Institut für Anorganische Chemie und Strukturchemie, Heinrich-Heine-Universität Düsseldorf, 40204 Düsseldorf, Germany. Tel: +49-211-81-12286. E-Mail: janiak@uni-duesseldorf.de

Emails: alex.spiess@uni-duesseldorf.de; jawie113.1@gmail.com; Egor.iwaschko@outlook.de; dennis.woschko@hhu.de

Contents

1. Chemicals

Table S1 List of used chemicals, including purity and supplier.

Chemical	**Purity**	**Supplier**
Pine wood rod, Ø = 14 mm		Local *Toom* hardware store[a]
NaOH, microgranules	≥ 99.5 %	ChemSolute
Maleic anhydride	≥ 99.5 %	Carl Roth
(3-aminopropyl)triethoxysilane	98 %	abcr
Zinc nitrate hexahydrate	98 %	Acros Organics
2-Methylimidazole	99 %	J&K Scientific
Aluminum nitrate nonahydrate	≥ 98 %	Carl Roth
Terephthalic acid	≥ 98 %	Alfa Aesar
Dimethylformamide	≥ 99.8 %	Honeywell
Methylene blue x-hydrate	High purity, biological stain	Alfa Aesar
Benzaldehyde	> 98 %	Acros Organics
Malononitrile	99 %	abcr
Toluene, anhydrous	99.8 %	Sigma Aldrich
Benzylidenmalononitrile	> 98 %	TCI
Aluminum standard for AAS,	999±5 mg L^{-1}	Sigma Aldrich
Zinc standard for AAS	1000±4 mg L^{-1}	Sigma Aldrich

[a] https://de.wikipedia.org/wiki/Toom_Baumarkt

2. Previously reported MOF@wood materials

Table S2 Previously reported MOF@wood composite materials.

Composite	MOF-loading [wt-%]	Application	Note	Ref.
ZIF-8@Beech	1.8	CO_2 adsorption, increased mechanical stability	Also reported HKUST-1@Beech	1
HKUST-1@Bamboo/Balsa	n.a.	Increased antibacterial properties		2
UiO-66@Basswood	2.2	Water purification		3
ZIF-8@PDA@Balsa	n.a.	Solar steam generation, water purification		4
AgPd@UiO-66@Poplar	3.2	Continuous hydrogen generation		5
ZIF-8@Basswood	4	Iodine capture		6
UiO-66-NH_2@MW-Balsa	49.6	Water purification	Wood pretreated with magnetic Fe_2O_3-NPs, also reported composites with Al-fum, MIL-100(Fe) & HKUST-1	7

3. Wood disks, effect of surface smoothing, and composite materials

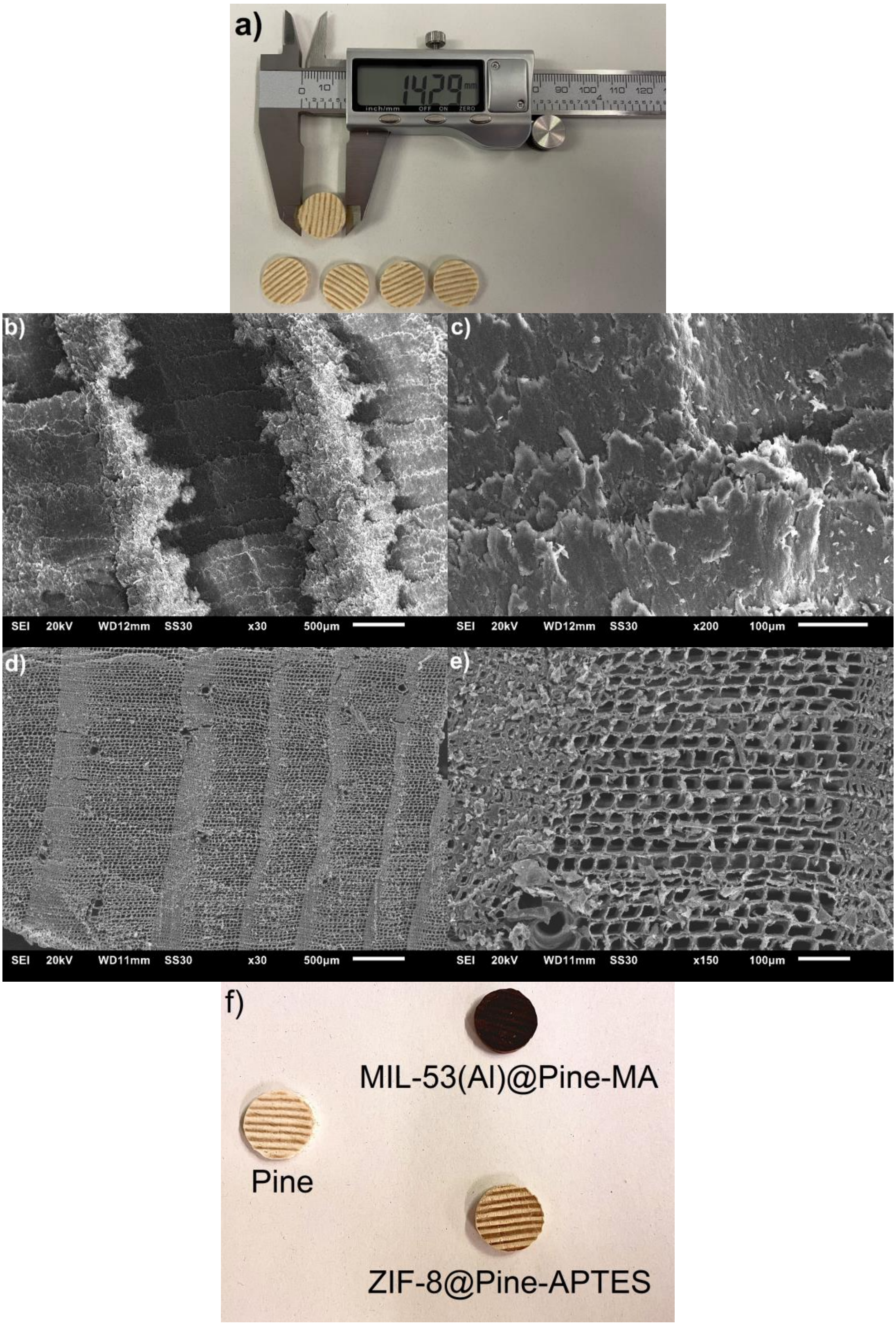

Fig. S1 a) Wood disks cut from a wood rod with a diameter of ~14 mm using a band saw. b, c) After cutting the wood on the band saw, the lumina are clogged in the surface. d, e) Surface planing opens the lumina again by removing a thin layer of wood with a sharp smoothing plane (plow or plough). f) Pictures of the composite materials MIL-53(Al)@Pine-MA and ZIF-8@Pine-APTES. After the synthesis, a dark discoloration can be observed for MIL-53(Al)@Pine-MA.

4. Wood functionalization: possible side reactions

During the wood functionalization with maleic anhydride (MA), the synthesis of mono-esters is the wanted reaction. However, it cannot be excluded that an unwanted di-esterification takes place. This reaction can be expected in two different ways, intra-chain and inter-chain di-esterification (Scheme S1a) where the second esterification either takes place within the same cellulose strain (intra-chain) or with a second strain (inter-chain).[8] In the case of APTES functionalization, there are more possible side reactions taking place (Scheme S1b). After the reaction with a first molecule of APTES, a polymerization of APTES molecules is possible, which can happen vertically (polymerization away from the substrate surface) or horizontally (polymerization on the substrate surface). The two polymerizations, however, are not necessarily unwanted, since they still introduce additional amino-groups. Besides that, there are different possible hydrogen-bridge formations which either make the amino groups unavailable for later coordination or create a weaker bond between the APTES molecule and the substrate surface. These are unwanted side reactions.[9]

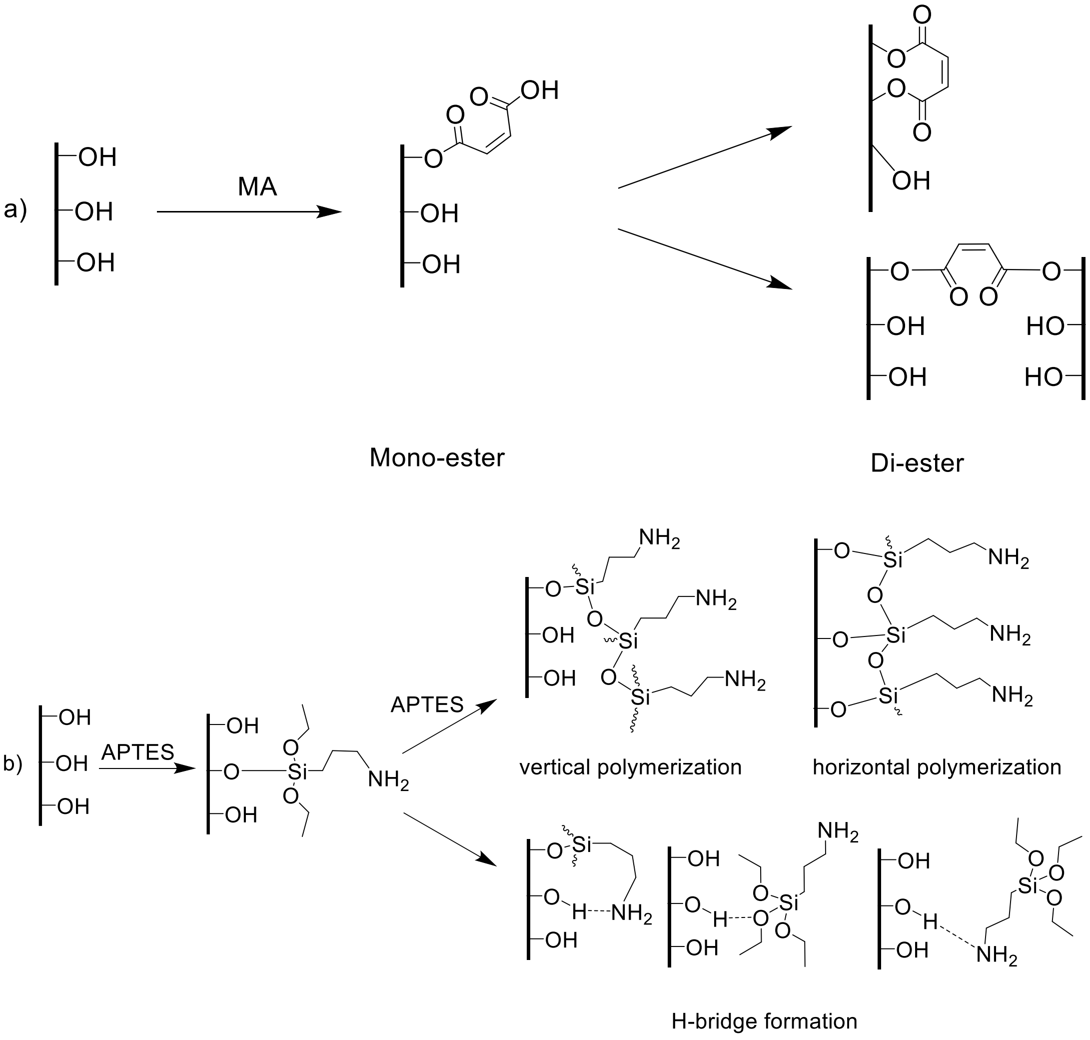

Scheme S1 a) Possible side reactions during wood functionalization with maleic anhydride. b) Possible side reactions during wood functionalization with (3-aminopropyl)triethoxysilane.

5. Structure description of MIL-53(Al) and ZIF-8

MIL-53(Al) is constructed of infinite chains of $AlO_4(OH)_2$ octahedra, which are interconnected by the terephthalate linker (BDC^{2-}), where each linker molecule is connected to four different Al-ions. The flexible structure is known for its breathing behavior, transitioning between the low temperature (*lt*) form with pore dimensions of 2.6 × 13.6 Å and the high temperature (*ht*) form with pore dimensions of 8.5 × 8.5 Å.[10] The MIL-53-type structure can not only be obtained with Al(III) ions, but with Fe(III) and Cr(III) ions as well. The transition between the *ht*- and *lt*-form is governed by the presence or absence of guest molecules within the structure. A fully activated MIL-53(Al) containing no guest molecules leads to the formation of the large-pore *ht*-form, while the adsorption of guest molecules like atmospheric water leads to the transition to the narrow-pore *lt*-form.[10,11,12,13]

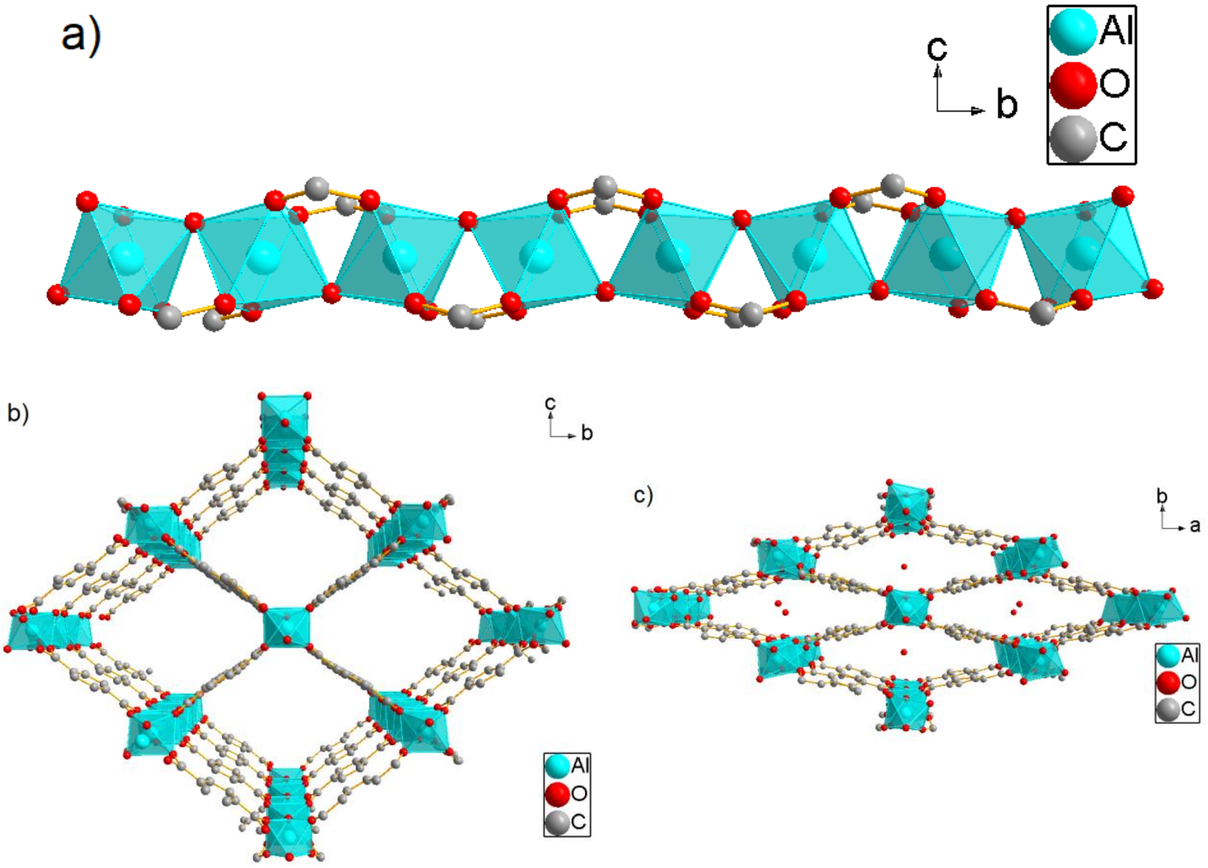

Fig. S2 a) Infinite chain of $AlO_4(OH)_2$ octahedra. b) Interconnected chains to form MIL-53(Al) in the *ht*-form. c) Interconnected chains to form MIL-53(Al) in the *lt*-form including water as guest molecule in the channels. In all cases hydrogen-atoms are omitted for clarity. The structures were produced using the Diamond software from the cif-file for MIL-53(Al) (Refcodes SABVUN and SABWAU, Ref. 10).

ZIF-8 is constructed of tetrahedrally coordinated Zn^{2+} ions interconnected by 2-methylimidazole as linker, creating a permanently porous structure with a pore diameter of 11.6 Å and a pore aperture diameter of 3.4 Å.[14,15] The structure of ZIFs is similar to those of zeolites, hence the name “zeolitic imidazolate framework”. ZIF-8 forms a sodalite (*sod*) network with hexagonal and quadratic faces. The 3.4 Å pore aperture is limited by the hexagonal faces while the single *sod*-cages are interconnected by the quadratic faces.[15,16]

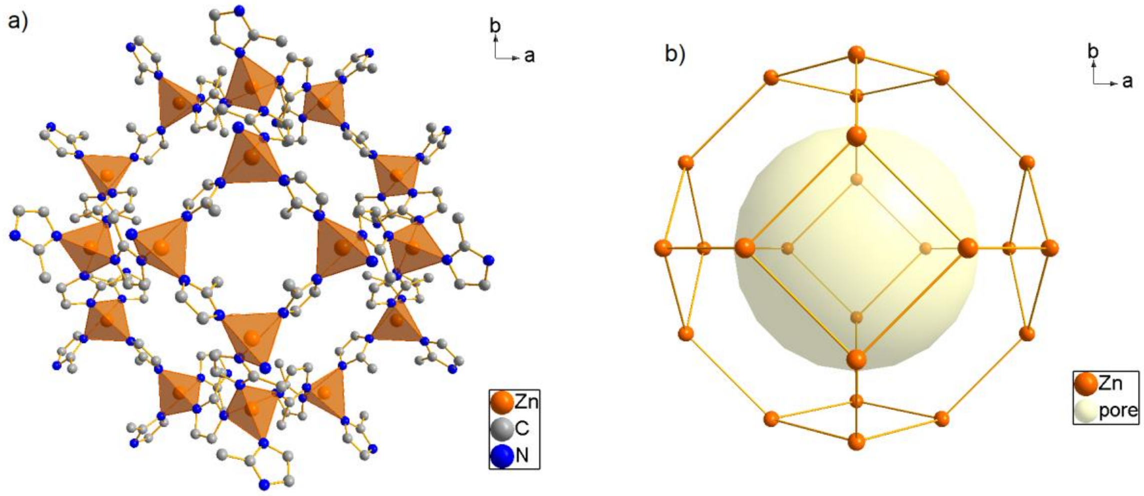

Fig. S3 a) 3D-framework structure of ZIF-8 showing the ZnN_4 tetrahedra. Hydrogen-atoms are omitted for clarity. b) One of the *sod*-cages with topological lines between the Zn atoms showing the hexagonal and quadratic faces. Inside the cage, the pore is highlighted in yellow. The structures were produced using the Diamond software from the cif-file for ZIF-8 (Refcode FAWCEN, Ref. 16).

6. IR-spectroscopy

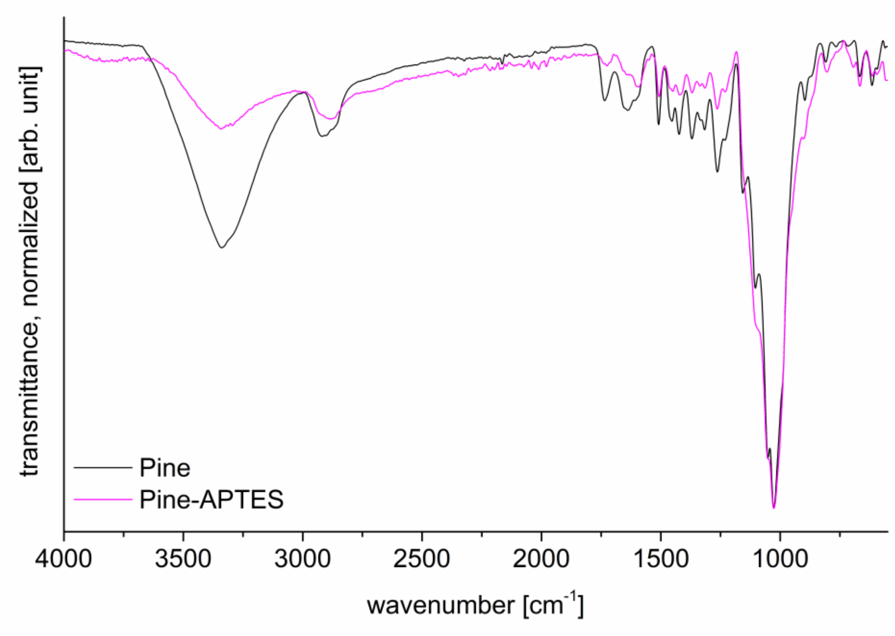

Fig. S4 ATR-IR spectrum of Pine-APTES compared to the pristine wood.

7. SEM Images

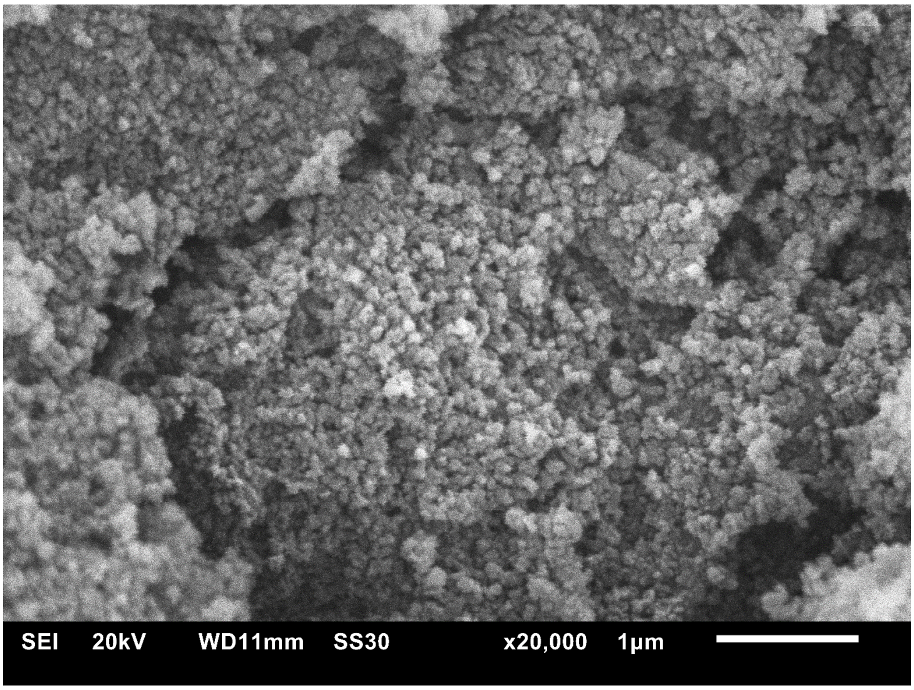

Fig. S5 SEM picture of the synthesized MIL-53(Al) showing the resulting nano-crystallites.

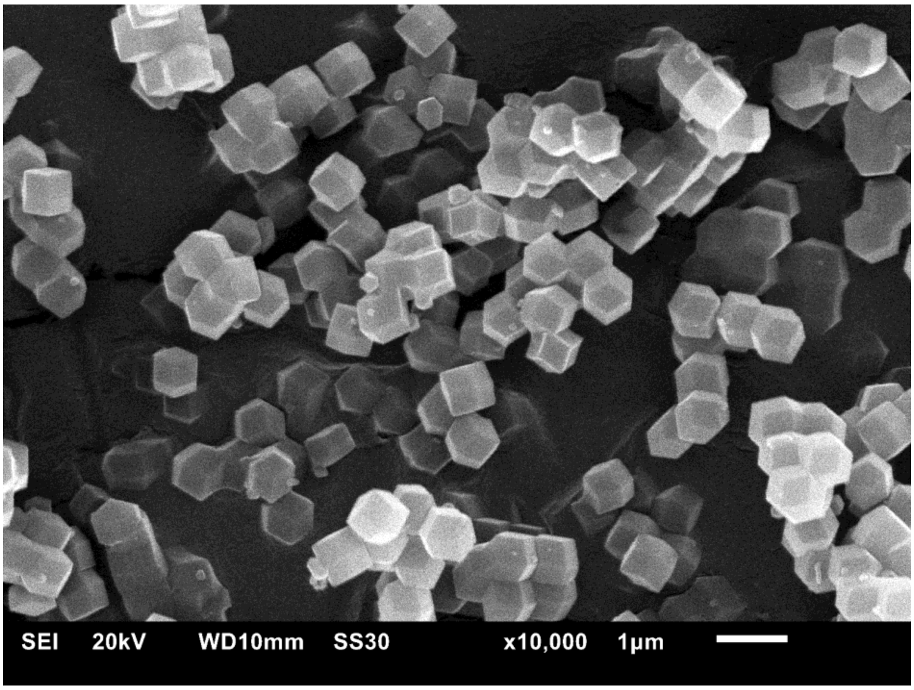

Fig. S6 SEM picture of the synthesized ZIF-8.

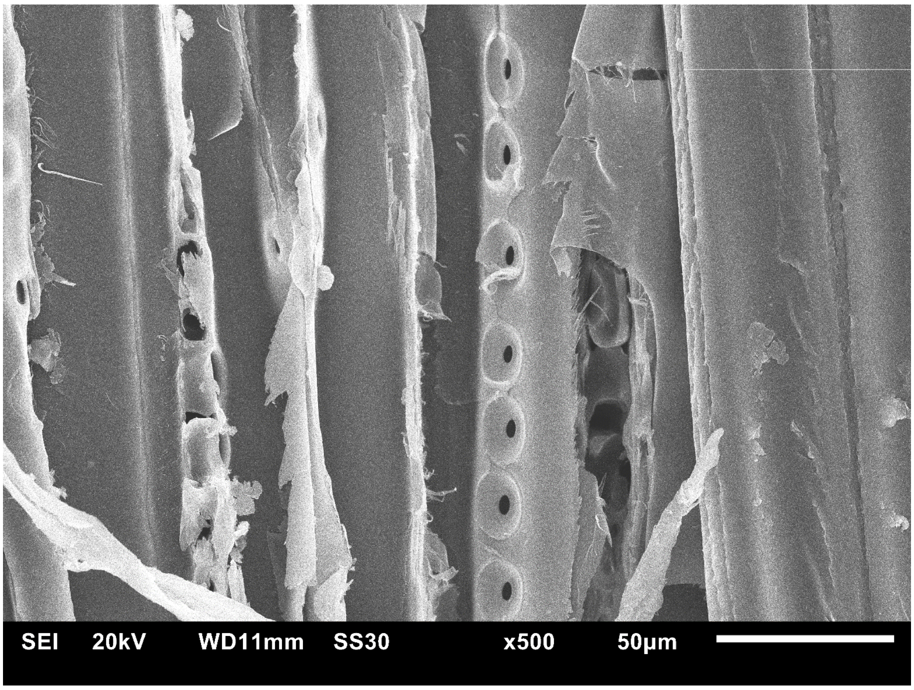

Fig. S7 SEM picture of pristine pine wood. The growth direction of the lumina is from top to bottom. The round holes which can be seen in the center of the picture are the pits (the connecting element between two lumina).

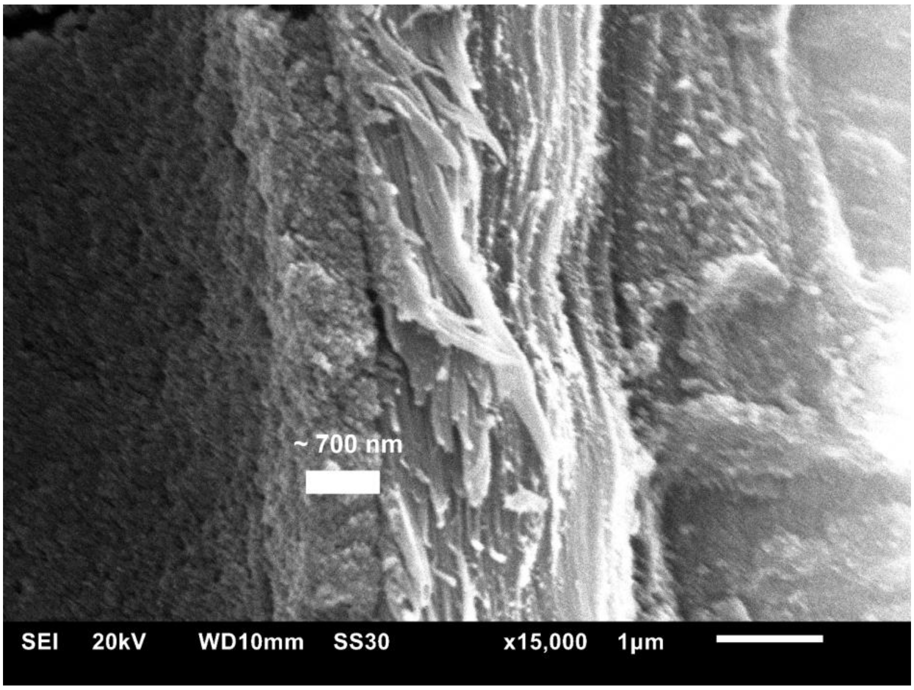

Fig. S8 MIL-53(Al)@Pine-MA. Picture showing the thickness of the MOF layer on the surface of the lumen.

8. Nitrogen-sorption pore-size-distribution

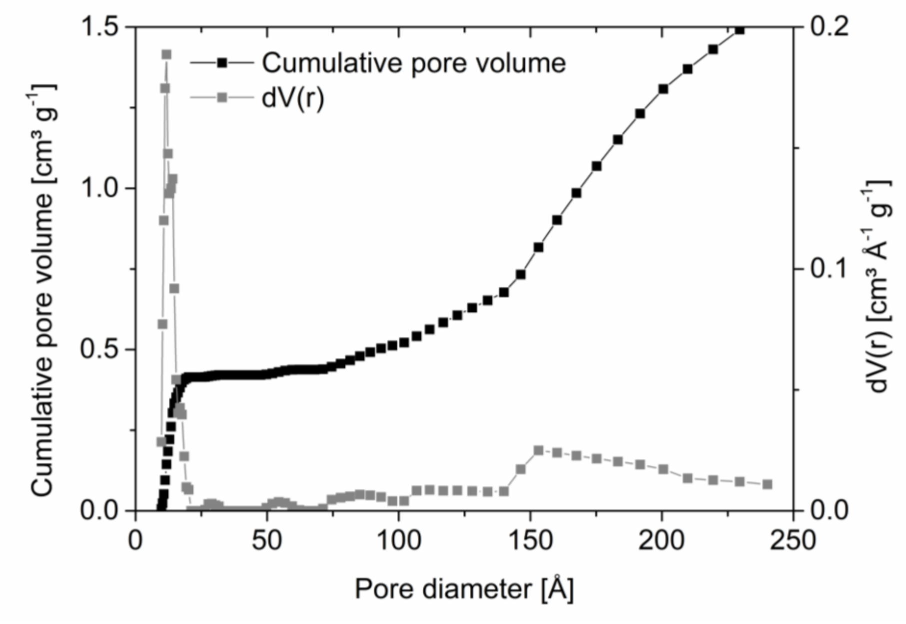

Fig. S9 Pore size distribution of the synthesized MIL-53(Al).

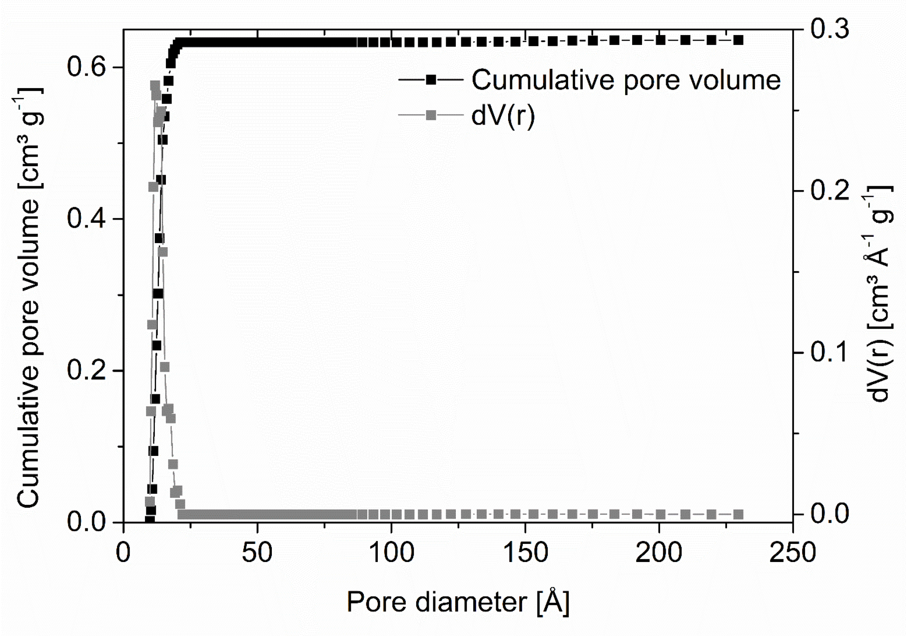

Fig. S10 Pore size distribution of the synthesized ZIF-8.

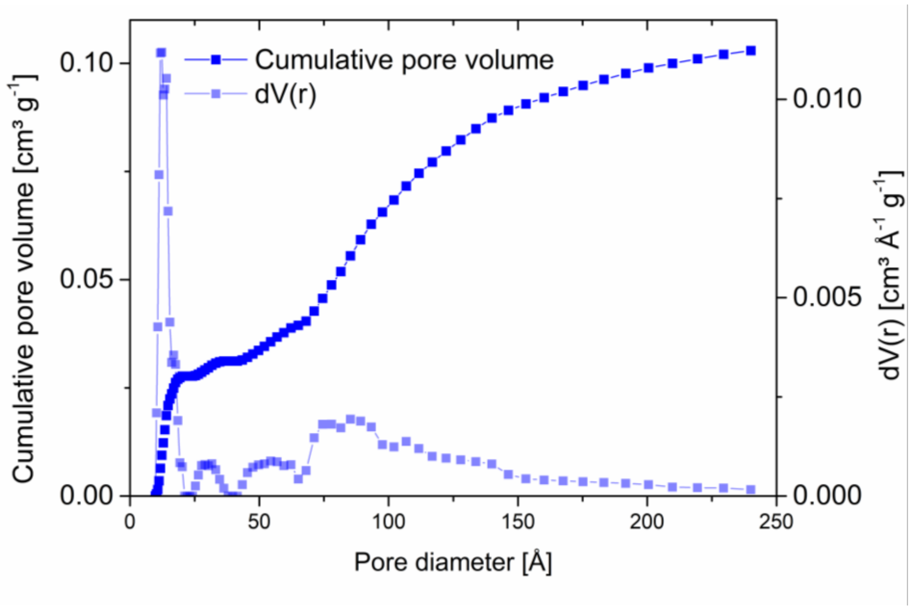

Fig. S11 Pore size distribution of the synthesized MIL-53(Al)@Pine-MA.

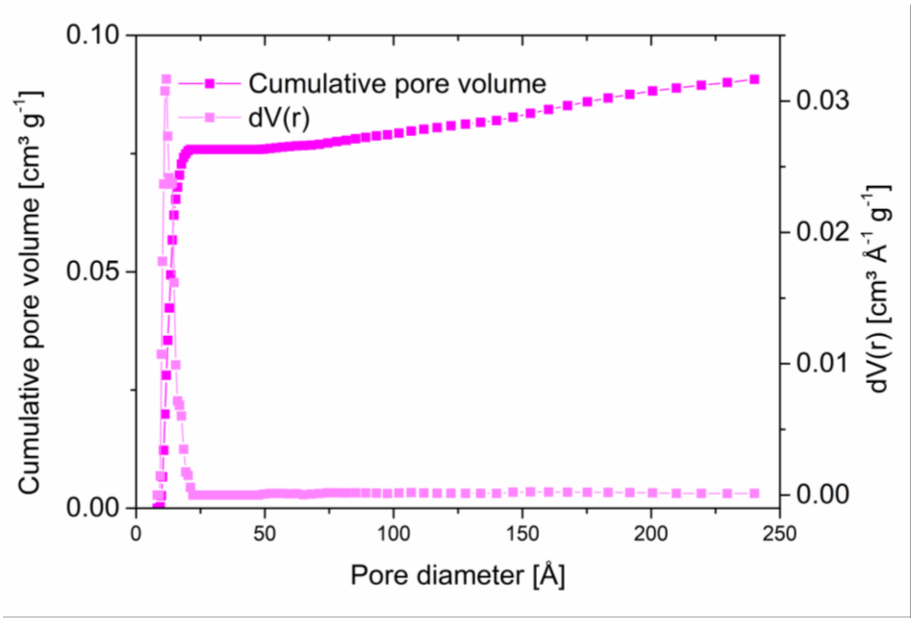

Fig. S12 Pore size distribution of the synthesized ZIF-8@Pine-APTES.

9. Calculation of MOF amount from BET results

The amount of MOF incorporated into the matrix can be estimated by its BET surface area, assuming that it is composed by the mass-averaged BET surface areas of the single components with their weight-percentage in the composite (Equation 1).[17] Since the wood matrix itself does not have a significant BET surface area (the measured BET surface lies within the experimental error), it can be assumed that the BET surface of the composite is only a result of the incorporated MOF, hence Equation 1 can be simplified to Equation 2 to calculate the weight-percentage of MOF inside the composite.

$$\mathrm{BET_{comp}}=\frac{\text{wt\% of matrix}}{100}*\mathrm{BET_{matrix}}+\frac{\text{wt\% of MOF}}{100}*\mathrm{BET_{MOF}} \qquad (1)$$

$$\mathrm{BET_{comp}}=\frac{\text{wt\% of matrix}}{100}*0\ \mathrm{m^2g^{-1}}+\frac{\text{wt\% of MOF}}{100}*\mathrm{BET_{MOF}} \rightarrow \text{wt\% of MOF}=\frac{\mathrm{BET_{comp}}}{\mathrm{BET_{MOF}}}*100 \qquad (2)$$

10. Methylene Blue adsorption

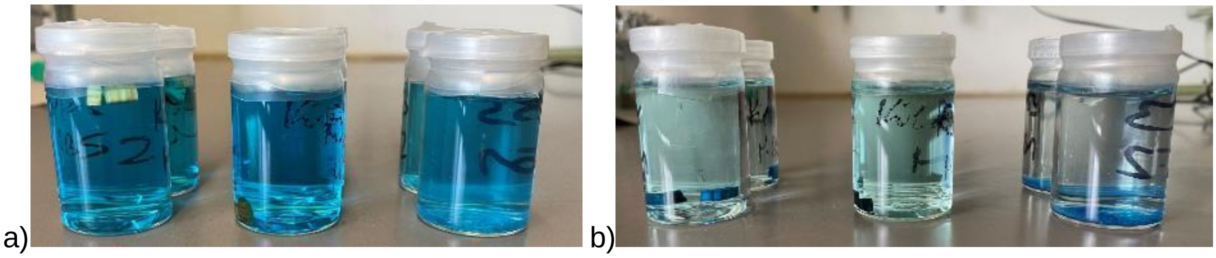
a) b)

Fig. S13 Methylene Blue adsorption (20 ml solution with 5 mg L^{-1}) of the reference materials a) at the beginning and b) after 48 h. From left to right: Pine, Pine-MA, MIL-53(Al).

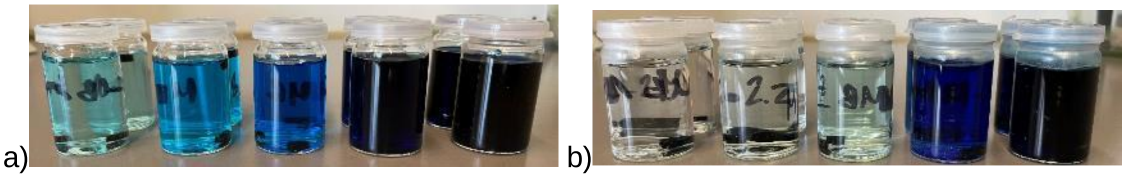
a) b)

Fig. S14 Adsorption of MB solutions with different concentrations (20 ml each) by MIL-53(Al)@Pine-MA a) at the beginning and b) after 48 h. From left to right: 1 mg L^{-1}, 5 mg L^{-1}, 10 mg L^{-1}, 100 mg L^{-1}, 250 mg L^{-1}. The solution with a concentration of 500 mg L^{-1} is not shown.

Fig. S15 MB adsorption kinetics of MIL-53(Al)@Pine-MA (50 ml MB solution with 5 mg L^{-1}). From left to right: start, 1 h, 2 h, 8 h, 24 h, 32 h, 48 h.

10.1 Determination of adsorption isotherms

For the determination of MB adsorption isotherms, the composite material MIL-53(Al)@Pine-MA was immersed in MB solutions with different concentrations (1 mg L^{-1}, 5 mg L^{-1}, 10 mg L^{-1}, 100 mg L^{-1}, 250 mg L^{-1} and 500 mg L^{-1}) for 48 h (Fig. S14). For every concentration, the experiment was performed in duplicate. The resulting isotherm was then fitted with both the Langmuir model (Equations 3-4) and the Freundlich model (Equations 5-6).

Langmuir model: $$q_e=\frac{k_L*q_{max}*c_e}{1+k_L*c_e} \quad (3)$$

linearized Langmuir model: $$\frac{c_e}{q_e}=\frac{1}{q_{max}*k_L}+\frac{c_e}{q_{max}} \quad (4)$$

Freundlich model: $$q_e=k_F*c_e^{(n)} \quad (5)$$

linearized Freundlich model: $$\log(q_e)=\log(k_F)+\frac{1}{n}*\log(c_e) \quad (6)$$

In both models, q_e represents the adsorbed amount of MB at equilibrium [mg g^{-1}], q_{max} the the maximum capacity [mg g^{-1}] and c_e the concentration of MB remaining in solution at equilibrium [mg L^{-1}]. For the Langmuir model k_L is the Langmuir constant [L mg^{-1}], while for the Freundlich model k_F represents the Freundlich constant [mg^{1-n} L^n g^{-1}] and n is a number $n \geq 0$ indicating the isotherm type.[18]

The determined MB adsorption isotherm is shown in Fig. S16a. For the three lowest concentrations, the MB is nearly completely adsorbed. After immersion in the solution with 500 mg L^{-1} of MB, the sorption capacity reaches 54 mg g^{-1}. The resulting isotherm was fitted to the Langmuir model (Fig. S16b) and the Freundlich model (Fig. S16c). None of the models shows a clearly better fit to the isotherm than the other, hence the adsorption cannot be clearly described by one model. When the resulting parameters from the fits are used to calculate q_e from c_e (Fig. S16a), it can be seen that the Freundlich model seemingly better describes the lower concentrations, while the Langmuir model seemingly better fits the higher concentrations.

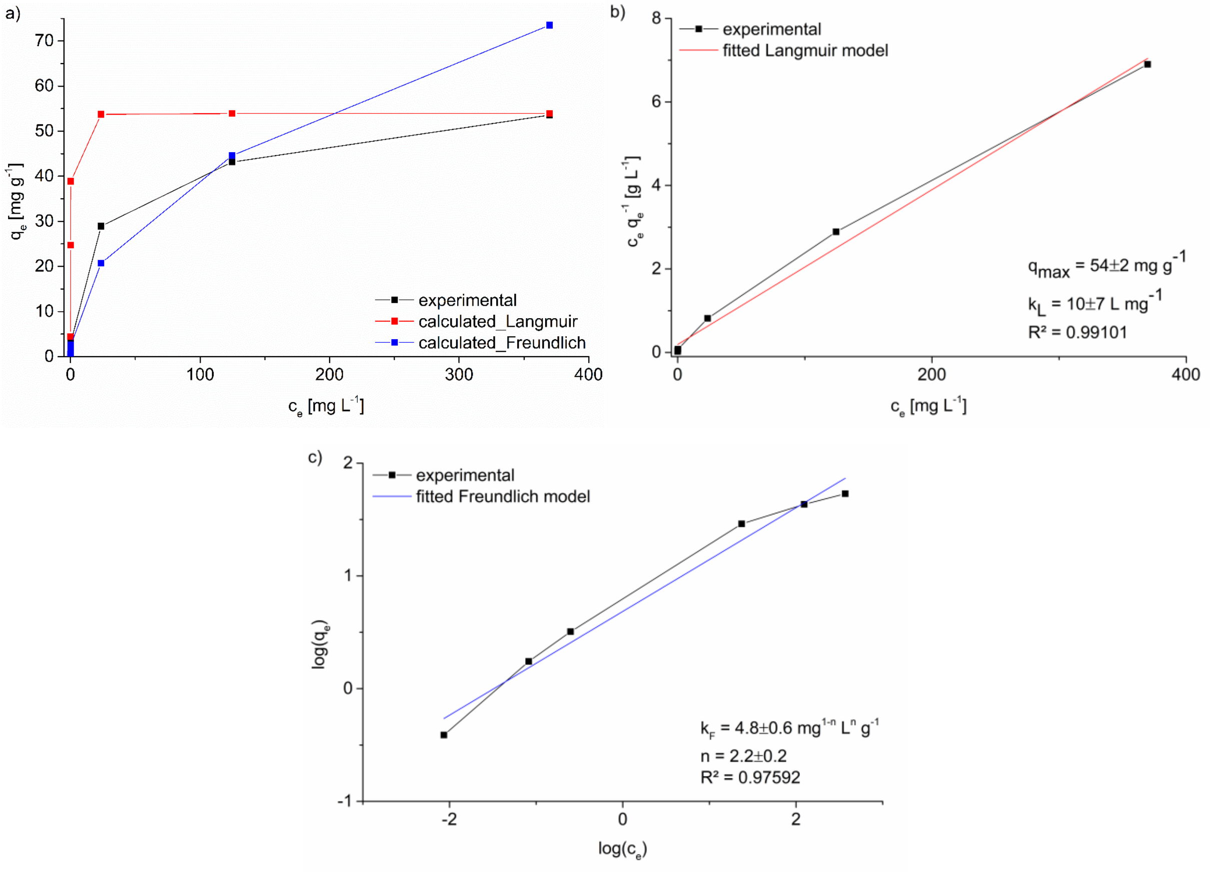

Fig. S16 a) Determined MB sorption isotherm of MIL-53(Al)@Pine-MA including calculated isotherms using the parameters obtained by fitting to b) the Langmuir model and c) the Freundlich model.

11. MOF content by TGA and SEM-EDX

We carried out a TGA for the composites with the highest MOF-loadings, i.e. ZIF-8@Pine-APTES and MIL-53(Al)@Pine-MA (Fig. S17). For ZIF-8@Pine-APTES, there will not only remain ZnO, but also SiO_2. From the residual mass of 12.5±0.5 wt-% the ZIF-8@Pine-APTES composite (ZnO+SiO_2) and the functionalized wood Pine-APTES (8.5±0.5 wt-% SiO_2 only), a MOF loading of 12.1±1.2 wt-% can be calculated, where the value corresponds well with the BET and AAS results. At the same time, we have to consider that TGA has a high error margin of ±0.5 wt% points and possibly even more in the low residual wt-% region. For MIL-53(Al)@Pine-MA, the residual Al_2O_3 TGA mass of 1.4±0.5 wt-% gives a MOF loading of 6±2 wt-%. At the same time, we tried to use SEM-EDX (despite its limitations, e.g. no H atom detection) for the determination of the Al content (Fig. S18). From the EDX spectra of two large areas an average MIL-53(Al) MOF content of 13.1 wt-% was calculated.

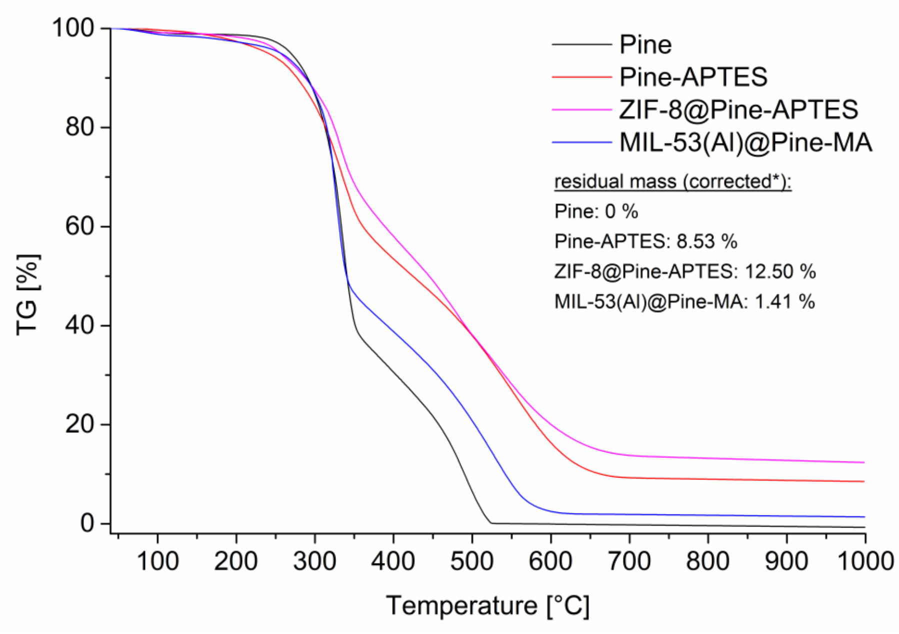

Fig. S17 Thermogravimetric analysis for the determination of residual metal oxide to determine the MOF content. In order to correct for the initial solvent loss, the mass percent at 150 °C was set to 100% and the residual mass corrected accordingly.

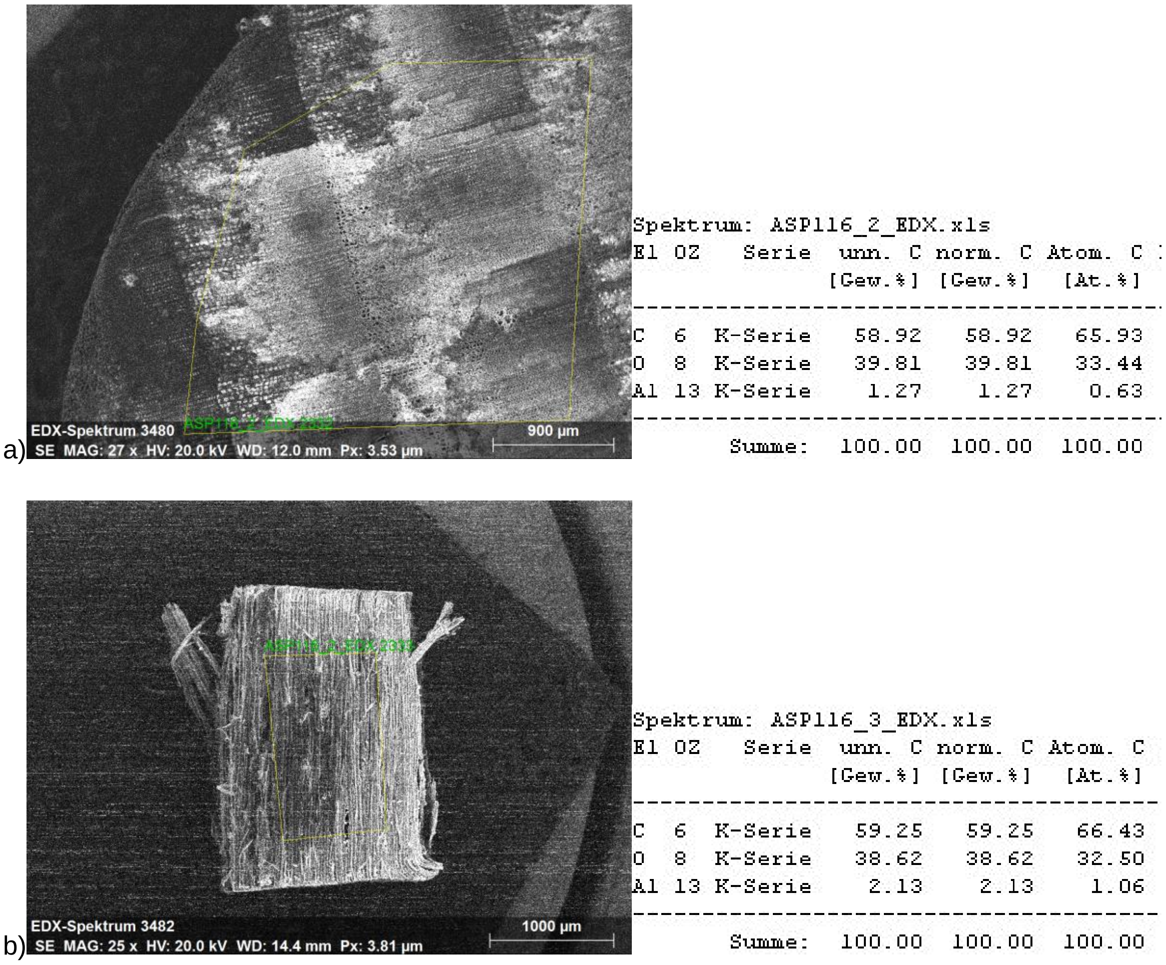

```
Spektrum: ASP116_2_EDX.xls
El OZ   Serie  unn. C norm. C Atom. C
               [Gew.%] [Gew.%]  [At.%]
---------------------------------------
C  6  K-Serie   58.92   58.92   65.93
O  8  K-Serie   39.81   39.81   33.44
Al 13 K-Serie    1.27    1.27    0.63
---------------------------------------
       Summe:  100.00  100.00  100.00
```

```
Spektrum: ASP116_3_EDX.xls
El OZ   Serie  unn. C norm. C Atom. C
               [Gew.%] [Gew.%]  [At.%]
---------------------------------------
C  6  K-Serie   59.25   59.25   66.43
O  8  K-Serie   38.62   38.62   32.50
Al 13 K-Serie    2.13    2.13    1.06
---------------------------------------
       Summe:  100.00  100.00  100.00
```

Fig. S18 SEM images with area for element composition. Hydrogen atoms cannot be accounted for. The MIL-53(Al) MOF content from the Al wt-% (Gew.%) in spectrum (a) is 9.8 wt-%, in spectrum (b) 16.4 wt-%, giving an average of 13.1 wt-%.

12. References

1 K. Tu, B. Puértolas, M. Adobes-Vidal, Y. Wang, J. Sun, J. Traber, I. Burgert, J. Pérez-Ramírez and T. Keplinger, *Adv. Sci.*, 2020, **7**, 1902897.

2 M. Su, R. Zhang, H. Li, X. Jin, J. Li, X. Yue and D. Qin, *RSC Adv.,* 2019, **9**, 40277–40285.

3 R. Guo, X. Cai, H. Liu, Z. Yang, Y. Meng, F. Chen, Y. Li and B. Wang, *Environ. Sci. Technol.,* 2019, **53**, 2705–2712.

4 Y. Lu, D. Fan, Z. Shen, H. Zhang, H. Xu and X. Yang, *Nano Energy,* 2022, **95**, 107016.

5 K. Tu, S. Büchele, S. Mitchell, L. Stricker, C. Liu, C. Goldhahn, J. Allaz, Y. Ding, R. Günther, Z. Zhang, J. Sun, S. Stucki, G. Panzarasa, S. C. Zeeman, I. Burgert, J. Pérez-Ramírez and T. Keplinger, *ACS Appl. Mater. Interfaces,* 2022, **14**, 8417–8426.

6 Z. Wang, Y. He, L. Zhu, L. Zhang, B. Liu, Y. Zhang and T. Duan, *Mater. Chem. Phys.,* 2021, **258**, 123964.

7 G. Huang, C. Huang, Y. Tao and H. Li, *Appl. Surf. Sci.,* 2021, **564**, 150325.

8 C.-A. Teacă, R. Bodîrlău and I. Spiridon, *Cellul. Chem. Technol.,* 2014, **48**, 863–868.

9 M. Zhu, M. Z. Lerum and W. Chen, *Langmuir,* 2012, **28**, 416–423.

10 T. Loiseau, C. Serre, C. Huguenard, G. Fink, F. Taulelle, M. Henry, T. Bataille and G. Férey, *Chem. Eur. J.,* 2004, **10**, 1373–1382.

11 C. Serre, F. Millange, C. Thouvenot, M. Nogues, G. Marsolier, D. Louer and G. Férey, *J. Am. Chem. Soc.*, 2002, **124**, 13519-13526.

12 F. Millange, C. Serre and G. Férey, *Chem. Commun*., 2002, **8**, 822-823.

13 F. Millange, N. Guillou, R. I. Walton, J.-M. Greneche, I. Margiolaki and G. Férey, *Chem. Commun.*, 2008, **39**, 4732-4734.

14 X.-C. Huang, Y.-Y. Lin, J.-P. Zhang and X.-M. Chen, *Angew. Chem. Int. Ed.,* 2006, **45**, 1557–1559.

15 . S. Park, Z. Ni, A. P. Côté, J. Y. Choi, R. Huang, F. J. Uribe-Romo, H. K. Chae, M. O'Keeffe and O. M. Yaghi, *Proc. Natl. Acad. Sci. U.S.A.,* 2006, **103**, 10186–10191.

16 W. Morris, C. J. Stevens, R. E. Taylor, C. Dybowski, O. M. Yaghi and M. A. Garcia-Garibay, *J. Phys. Chem. C,* 2012, **116**, 13307–13312.

17 M. Wickenheisser, A. Herbst, R. Tannert, B. Milow and C. Janiak, *Microporous Mesoporous Mater*., 2015, **215**, 143-153.

18 B. Moll, T. Müller, C. Schlüsener, A. Schmitz, P. Brandt, S. Öztürk and C. Janiak, *Mater. Adv.,* 2021, **2**, 804-812.